Prediction of Zenith Tropospheric Delay in GNSS Application Using Machine Learning Models

Appau, K. J.,[1*] Yakubu, I.[2] and Ziggah, Y. Y.[3]
Geomatic Engineering Department, University of Mines and Technology, Ghana
E-mail: kappaujunior@umat.edu.gh,[1*] yissaka@umat.edu.gh,[2] yyziggah@umat.edu.gh[3]
**Corresponding Author*

DOI: https://doi.org/10.52939/ijg.v21i8.4371

Abstract
Accurate estimation of Zenith Tropospheric Delay (ZTD) is essential for enhancing the accuracy of Global Navigation Satellite System (GNSS) positioning and atmospheric modelling. Traditional tropospheric delay models, including numerical weather models, analytical models, and empirical approaches, often struggle to capture the complex nonlinear variations in ZTD. To overcome these limitations, this study explores the use of five machine learning models (Kolmogorov–Arnold Network (KAN), Long Short-Term Memory (LSTM), Multilayer Perceptron Neural Network (MLPNN), Extreme Gradient Boosting (XGBoost), and Random Forest) to predict ZTD across four GNSS COR stations in Ghana: Accra, Ho, Kumasi, and Akim Oda. Meteorological parameters (pressure, temperature, and relative humidity) and geospatial features (latitude and ellipsoidal height) were utilised as input variables. Model performance was assessed using Root Mean Square Error (RMSE), Mean Absolute Error (MAE), and the Coefficient of Determination (R^2). Results showed that the KAN model consistently outperformed all other models, achieving test RMSEs of approximately 10 mm and R^2 above 0.976, demonstrating its capacity to model nonlinear and sequential atmospheric patterns with interpretability and efficiency. LSTM and MLPNN also yielded competitive results, while ensemble methods, particularly Random Forest, lagged in generalisation and accuracy. The findings highlight the potential of interpretable deep learning techniques like KAN to improve GNSS-based atmospheric modelling and precise positioning applications in tropical regions.

Keywords: Ensemble Methods, GNSS Meteorology, KAN, Machine learning, Zenith Tropospheric Delay

1. Overview

The widespread deployment of Continuously Operating Reference Stations (CORS) has significantly enhanced Global Navigation Satellite System (GNSS) capabilities, enabling high-resolution geodetic studies of tectonic and non-tectonic processes, such as interseismic strain, postseismic deformation, and surface displacements. These analyses rely heavily on coordinate time series derived from continuous CORS data [1]. However, GNSS positioning accuracy is significantly affected by atmospheric delays, particularly Zenith Tropospheric Delay (ZTD), which can introduce errors of 2 to 22 m depending on satellite elevation angles [2]. To improve GNSS precision and support atmospheric water vapour monitoring, advanced tropospheric delay modelling techniques are essential [3][4][5][6][7][8] and [9].

Traditionally, tropospheric delay models are categorised into three main types: numerical weather models (NWMs), analytical models, and empirical models. NWMs, such as the European Centre for Medium-Range Weather Forecasts (ECMWF) [10][11] and [12] and the Global Forecast System (GFS) [13], estimate delays using global and regional atmospheric data. Analytical models utilise mathematical equations derived from direct meteorological observations, with prominent examples including the Hopfield [14], Saastamoinen [15], and Black [16] models. Empirical models are based on statistical analyses of historical atmospheric and GNSS data, such as the University of New Brunswick (UNB) series [17], the European Geostationary Navigation Overlay Service (EGNOS) model [18], the TropGrid models [19][20] and the Global Pressure and Temperature (GPT) series [21][22][23] and [24]. The traditional models for estimating tropospheric delay typically depend on single-function approaches for modelling and curve fitting. However, these methods struggle to accurately capture the inherently complex and nonlinear variations in tropospheric delay [25].

In contrast, machine learning models have demonstrated strong capabilities in approximating nonlinear functions, allowing for a more precise representation and prediction of these intricate variations. Various machine learning techniques have been effectively employed for tropospheric delay forecasting and have proven robust in this field. The most adopted methods include Artificial Neural Networks [26][27][28][29][30] and [31], Backpropagation Neural Networks (BPNN) [32] and [33], Long Short-Term Memory (LSTM) [34][35] and [36] and Multilayer Perceptron Neural Networks (MLPNN) [37].

While traditional deep learning models such as LSTM and MLP/ANN have demonstrated effectiveness in modelling nonlinear and temporal processes, they exhibit key limitations in scientific domains. LSTMs, for example, often suffer from data inefficiency, high sensitivity to hyperparameter tuning, and limited interpretability, particularly in applications with sparse or noisy observations [38]. Similarly, MLPs and other ANNs are prone to overfitting due to dense parameterisation and therefore offer limited transparency in how features influence predictions [39]. Ensemble methods such as Random Forest and XGBoost, while powerful in many structured learning tasks, lack native temporal modelling capabilities and rely heavily on post-hoc explanation tools due to their inherent model opacity [40].

Recently, the Kolmogorov–Arnold Network (KAN) has emerged as a novel neural architecture designed to improve interpretability and computational efficiency. Based on the Kolmogorov–Arnold representation theorem, it models multivariate functions through compositions of learnable, spline-based univariate transformations, enabling data-adaptive and locally interpretable function approximation [41]. KAN has demonstrated strong performance in complex scientific regression tasks using fewer parameters. For example, polynomial-enhanced KANs achieved accuracy comparable to MLP-based PINNs and DeepONets on PDE benchmarks while maintaining compact structures [42], and shallow KANs have outperformed MLPs in modelling physical systems with high accuracy and low complexity [43]. These attributes make KAN particularly suitable for modelling complex geophysical phenomena like Zenith Tropospheric Delay (ZTD), where interpretability, functional complexity, and data constraints are critical.

In view of the robust performance of the KAN, this study introduces KAN for Zenith Tropospheric Delay (ZTD) prediction for the first time and evaluates its performance against four widely used machine learning models including Long Short-Term Memory networks (LSTM) [44], Multilayer Perceptron Neural Networks (MLPNN) [37], Extreme Gradient Boosting (XGBoost) [45], and Random Forest [46]. These benchmark models have been successfully applied in prior ZTD prediction studies across various climatic zones, providing a solid basis for performance comparison and validation. By introducing KAN and systematically comparing it to established methods, this research aims to assess its applicability and potential advantages for GNSS meteorological modelling.

2. Tropospheric Delay in GNSS

GNSS systems, such as GPS, GLONASS, or BeiDou, rely on microwave signals transmitted from satellites to ground-based receivers. As these signals pass through the neutral atmosphere (troposphere), they experience delays due to variations in temperature, pressure, and water vapour content. This delay, known as tropospheric delay, consists of hydrostatic and wet components and affects both the carrier and code phases equally. These delays are particularly significant under high-humidity, low-pressure, and variable temperature conditions common in tropical regions. Figure 1 shows signal path delays in Global Navigation Satellite Systems.

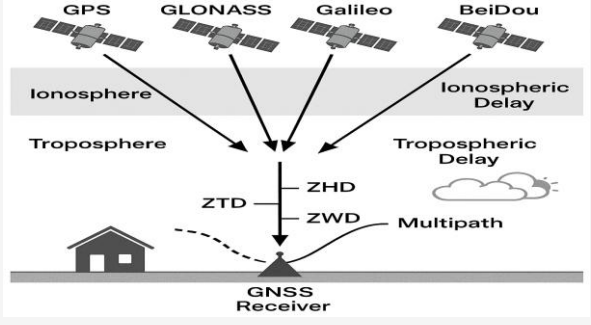

Figure 1: Signal path delays in Global Navigation Satellite Systems (GNSS)

The tropospheric delay is the additional delay in GNSS signals caused by the troposphere and is expressed in terms of total refractivity (N) [47]. The Zenith Tropospheric Delay (ZTD), comprising the Zenith Hydrostatic Delay (ZHD) and Zenith Wet Delay (ZWD), represents the total delay in the zenith direction. ZHD, which makes up about 90% of ZTD, is accurately estimated using surface meteorological data, whereas ZWD is highly variable due to atmospheric moisture dynamics [48][49] and [50]. Since the troposphere is non-dispersive below 15 GHz, it affects all GNSS frequencies uniformly, influencing both carrier and code signals [51].

The atmospheric refractive index mainly governs this delay. The delay in the zenith direction is expressed as the path integral of refractivity N, as shown in Equation 1:

$$ZTD = 10^{-6}\int_0^{h_{top}} N(h)dh$$

Equation 1

Where:

$N = (n-1) \times 10^6$

h = altitude

h_{top} = neutral atmosphere (50 km to 100 km [52])

The refractivity N can be decomposed into two main components as depicted in Equation 2:

$$N = N_d + N_w$$

Equation 2

Where:

N_d = hydrostatic (dry) component

N_w = wet component.

These components are derived from atmospheric parameters, shown in Equation 3 [52]:

$$N_d = k_1 \frac{P}{T}, N_w = k_2 \frac{e}{T} + k_3 \frac{e}{T^2}$$

Equation 3

Where:

P = total atmospheric pressure (hPa)

T = absolute temperature (K)

e = the water vapour pressure

k_1 = 77.689 J/hPa

k_2 = 71.2952 K/hPa

k_3 = 375463 K^2/hPa

The total Zenith Tropospheric Delay is thus typically partitioned into two additive components, represented by Equation 4:

$$ZTD = ZHD + ZWD$$

Equation 4

Where:

ZHD = zenith hydrostatic delay

ZWD = zenith wet delay.

The hydrostatic delay constitutes about 90% of the total tropospheric delay and exhibits minimal variation over time and space. In contrast, the wet component is highly variable, primarily influenced by atmospheric water vapour content [53]. The Zenith Hydrostatic Delay (ZHD) can be calculated from surface pressure using the Saastamoinen model [54], represented by Equation 5:

$$ZHD = 0.0022768 \frac{P_\delta}{f(\phi, H)}$$

Equation 5

Where:

P_δ = surface atmospheric pressure at the station (hPa or mbar)

$Ø$ = Geodetic latitude of the station (in degrees)

H = ellipsoidal height in meters.

The function $f(Ø,H)$ accounts for the variation in gravity with latitude and elevation and is usually approximated using Equation 6:

$$f(Ø,H) = 1 - x\cos(2Ø)\ \ 0.00028H$$

Equation 6

Where:

x = 0.00266

This formulation assumes a hydrostatic equilibrium of the atmosphere and is widely used due to its accuracy and simplicity [54]. The zenith wet delay is associated with the partial pressure of water vapour and is defined by Equation 7:

$$ZWD = 10^{-6}\int_0^{h_{top}} (k_2 \frac{e}{T} + k_3 \frac{e}{T^2})dh$$

Equation 7

The terms used in Equation 7 are as defined in Equation 3.

3. Materials and Methods

3.1 Study Area

Ghana, located in West Africa, spans between latitudes 4.5° N and 11.5° N and longitudes 3.5° W and 1.5° E. It is bordered by Burkina Faso to the north, Côte d'Ivoire to the west, and Togo to the east, with the Gulf of Guinea forming its southern boundary along a 550 km stretch of the Atlantic coast. The Survey and Mapping Division (SMD) of the Lands Commission initially established five GNSS Continuously Operating Reference Stations (CORS) in Accra, Kumasi, Takoradi, Tamale, and Bolgatanga. Later, the Licensed Surveyors Association of Ghana (LiSAG) deployed eight additional CORS stations in Accra, Kumasi, Takoradi, Tarkwa, Koforidua, Akim Oda, Winneba, and Ho. Although the SMD-operated stations are currently inactive, the LiSAG stations remain operational. This study focuses on four of these active GNSS CORS sites, as illustrated in Figure 2.

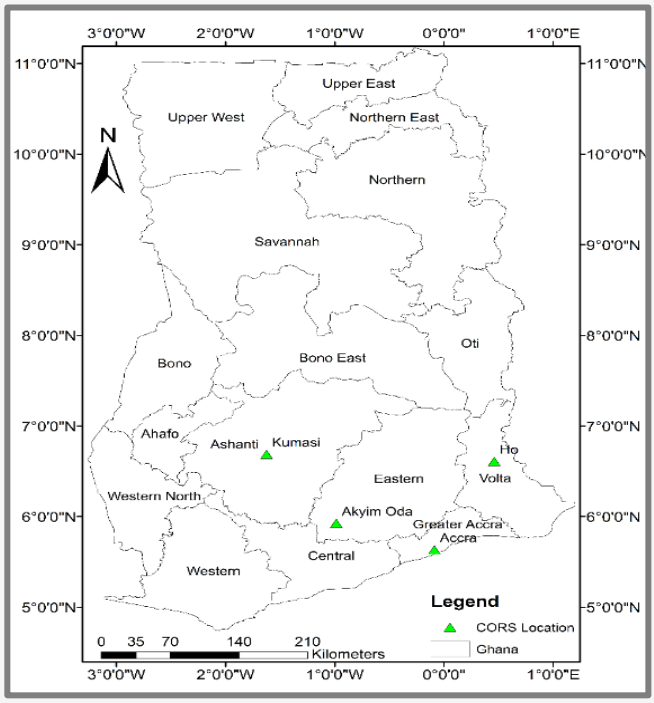

Figure 2: Location of selected GNSS CORS in Ghana

3.2 Dataset Description

The dataset employed in this study comprises GNSS observations from four Continuously Operating Reference Stations (CORS) located in Kumasi, Ho, Accra, and Akim Oda, covering the period from 2020 to 2022. The dataset includes RINEX observation files containing pseudorange and carrier phase measurements, which are essential for precise positioning, along with navigation files that provide satellite ephemeris data to support accuracy enhancement. To account for site-specific atmospheric influences, meteorological parameters such as temperature (°C), pressure (hPa), and relative humidity (%) were sourced from the Ghana Meteorological Agency at locations near the stations. The data were selected across well-defined time intervals to ensure comprehensive temporal coverage for Zenith Tropospheric Delay (ZTD) estimation. The use of dual-frequency GNSS receivers at all stations mitigates ionospheric delay, thereby improving the reliability of the derived ZTD values. Figure 3 illustrates the temporal distribution and availability of GNSS data across the four stations from 2020 to 2022, highlighting variations in data acquisition performance. ZTD estimation was performed using the PRIDE PPPAR software, which implements the Precise Point Positioning with Ambiguity Resolution (PPPAR) method.

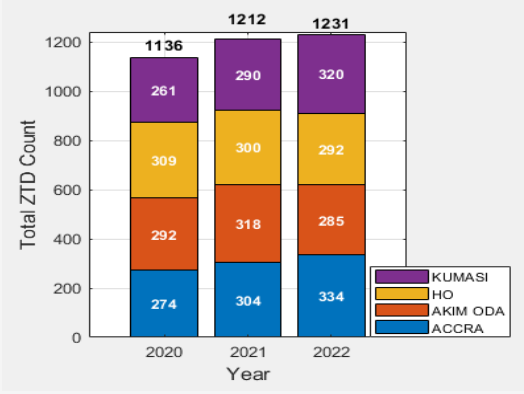

Figure 3: Data availability for the selected COR stations

Table 1 summarises the PPPAR strategies employed. ZTD values were computed at a temporal resolution of 30 seconds, and the daily mean ZTD was obtained by averaging all epoch-based ZTD values, as defined in Equation 8.

$$ZTD = \sum_{i=1}^{n} \frac{STD_i}{n}$$

Equation 8

Where:

n = the total number of epochs (2,880)

ZTD_i = the ZTD at each epoch

Table 1: Strategies implemented in the PRIDE PPPAR

Component	Strategy
Input Data	Dual-frequency GNSS (RINEX, L1/L2)
Observation Types	GPS/GLONASS raw pseudorange and carrier phase
Temporal Resolution	30 s
Positioning Mode	Static PPP (for fixed CORS stations)
Quality Control	Cycle slip detection/correction, configurable elevation cutoff (15°), outlier rejection via residual analysis
Clock and Orbit Corrections	IGS Final Precise Orbit and Clock products
Ionospheric Mitigation	Dual-frequency ionosphere-free linear combination
Ambiguity Resolution	LAMBDA method
Tropospheric Modelling	Saastamoinen model (ZHD) with pressure corrections; ZWD estimated using meteorological data; VMF3 for mapping function
Tidal Corrections	Solid Earth tides, ocean loading, pole tides (IERS conventions)
Antenna Corrections	IGS antenna phase centre offsets/variations (receiver and satellite)
Tropospheric Gradients	Estimated to account for horizontal asymmetries
Processing Strategy	Sequential least squares with Kalman filtering
Output	Total ZTD (metres)

3.3 Machine Learning Techniques

This study employed five machine learning (ML) techniques to develop predictive models for estimating Zenith Tropospheric Delay (ZTD). The selected methods include the Kolmogorov Arnold Network (KAN), Multi-Layer Perceptron Neural Network (MLPNN), Long Short-Term Memory (LSTM), Extreme Gradient Boosting (XGBoost), and Random Forest (RF). Model development for all techniques was conducted using MATLAB R2024, except for XGBoost, which was implemented in Python. The methodological workflow adopted in this study is illustrated in Figure 4. Detailed descriptions of the applied ML techniques are provided in the subsequent subsections.

3.3.1 Kolmogorov-Arnold Networks (KAN)

KAN is a neural architecture based on the Kolmogorov–Arnold representation theorem, which states that any continuous multivariate function can be represented as a finite sum of univariate function compositions [55]. This foundation allows KAN to simplify complex nonlinear relationships into interpretable components, improving model expressiveness and transparency. The mathematical expression of the theorem is given in Equation 9.

$$f(x_1,...,x_n) = \sum_{q=1}^{2n+1} \phi_q \left(\sum_{p=1}^{n} \phi_{q,p}\left(x_p\right) \right)$$

Equation 9

Where:

$\emptyset_{q,p}$ = univariate functions that map each input variable

x_p and $\emptyset_q$ = continuous functions. This allows KAN to model complex interactions dimensional data through compositions of simpler univariate functions

KAN builds on the Kolmogorov-Arnold representation theorem by replacing traditional fixed linear weights with adaptive, spline-based univariate functions. Unlike conventional MLPs that use fixed node activations, KAN employs learnable B-spline activation functions along edges, which are dynamically adjusted during training. This design enables more effective modelling of complex, nonlinear patterns. The mathematical form of a KAN layer is presented in Equation 10 as:

$$\emptyset = \{\emptyset_{q,p}\},\ p = 1, 2, \ldots, n_{in},\ q = 1, 2, \ldots, n_{out}$$

Equation 10

Where:

$\emptyset_{q,p}$ = parametrised functions with learnable parameters

KAN's structure enables it to model complex nonlinear relationships more effectively than traditional MLPs. To improve its representational power, deeper architectures have been introduced, formed by stacking multiple KAN layers in sequence [56]. The formulation of a deeper KAN is given in Equation 11:

$$KAN(x) = (\emptyset_{L-1}\ 0\ \emptyset_{L-2}\ 0\ \ldots\ 0\ \emptyset_0)(x)$$

Equation 11

Where:

$\emptyset_L$ = a *KAN* layer

Increasing the network depth enables *KAN* to learn more complex patterns and dependencies. Each layer L transforms the input x using learnable functions $\emptyset_{q,p}$ enhancing the model's flexibility and capacity. Table 2 outlines the *KAN* architecture and hyperparameters used in this study.

3.3.2 Long Short-Term Memory (LSTM)

LSTM networks are a variant of recurrent neural networks (RNNs) designed to overcome the vanishing gradient issue by using memory cells and gating mechanisms [56]. These include the input gate (managing new information), forget gate (handling past data retention), and output gate (controlling output flow). Equations 12–15 describe the LSTM cell's forward propagation.

$$i_t = \sigma(W_{ix}x_t + W_{ir}h_{t-1} + W_{ic}c_{t-1} + b_i)$$
Equation 12

$$f_t = \sigma(W_{fx}x_t + W_{fr}h_{t-1} + W_{fc}c_{t-1} + b_f)$$
Equation 13

$$C_t = f_tC_{t-1} + i_tg(W_{cx}x_t + W_{cr}h_{t-1} + b_c)$$
Equation 14

$$o_t = \sigma(W_{ox}x_t + W_{or}h_{t-1} + W_{oc}c_{t-1} + b_o)$$
Equation 15

Where:

t = current time
i_t = value of the input gate
f_t = value of forget gate
C_t = state of the current time's memory cell
o_t = value of output gate
h_{t-1} = output state of the previous hidden layer
σ = activation function of each node in the network, in which the sigmoid function is used

Table 3 also provides a detailed summary of the LSTM model architecture and the corresponding hyperparameter configurations used in this study.

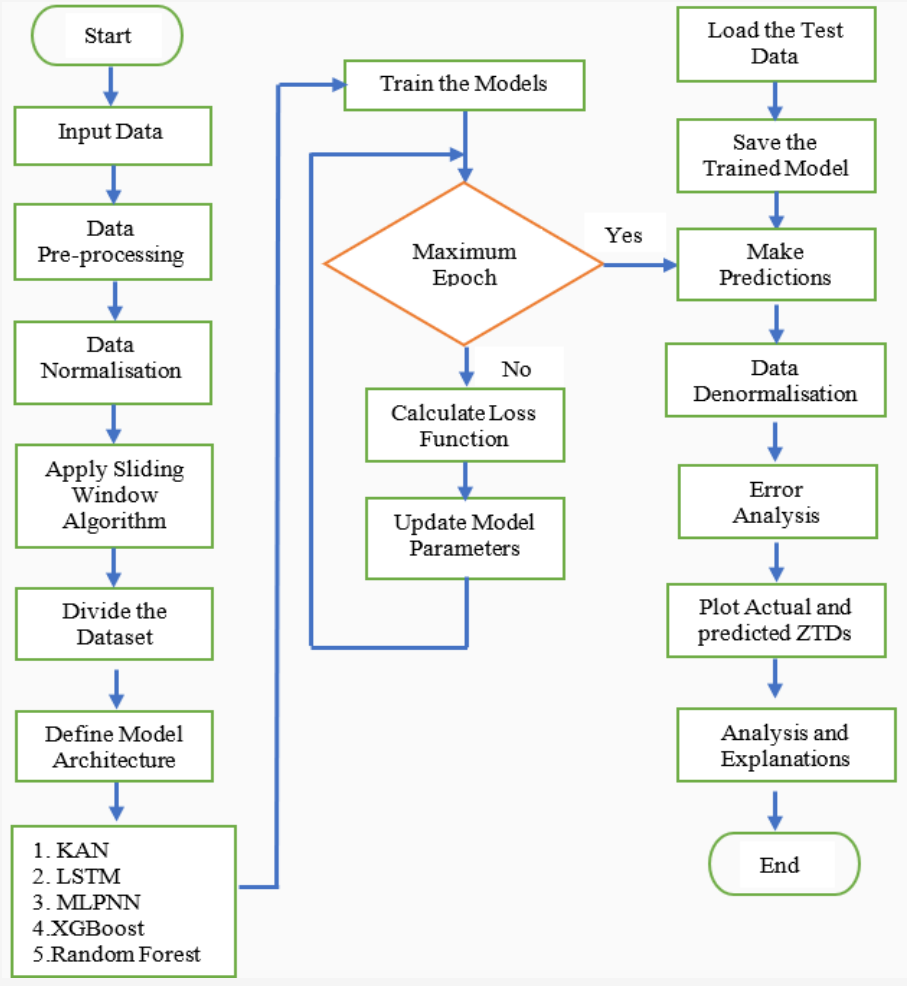

Figure 4: Schematic workflow for methodology

Table 2: Summary of model architecture and parameters for KAN

Component	Implemented Setting
Hierarchical Layers	3 Layers (Kolmogorov-Arnold Function Decomposition)
Intermediate Mixing	Learnable Weights λ_{pq} for feature interactions
Basis Functions	Multiple trainable univariate functions $Ø_q(x)$ per layer
Transformation Function	$Ø(x) = \alpha tanh(bx + c) + dx^2 + ex$
Output Aggregation	Summation over transformed inputs
Normalization	Min-Max Scaling
Optimization Algorithm	Adam (with dlgradient for backpropagation)
Loss Function	Mean Squared Error (MSE)
Batch Size	25 (Mini-Batch Training)
Learning Rate	0.005 (Adaptive Learning Rate)
Epochs	1,000

Table 3: Summary of model architectures and parameters for LSTM

Component	LSTM
Recurrent Layer	LSTM (128 neurons, last output mode)
Dropout Probability	0.3
Fully Connected Layer	64 neurons
Feature Scaling	Min-Max Normalisation
Activation Function	Swish
Batch Size	25
Optimizer	Adam
Learning Rate	0.01
Epochs	1,000

3.3.3 Multilayer Perceptron Neural Network (MLPNN)

MLPNN is a widely adopted ANN architecture known for its effectiveness in nonlinear regression and classification tasks [57]. It comprises an input layer, one or more hidden layers, and an output layer, with each neuron computing a weighted sum of its inputs followed by an activation function, as shown in Equation 16.

$$X = \left(\sum_{i=1}^{n} w_{ij} x_i \right) + b_j$$

Equation 16

Where:

w_{ij} = interconnecting weights of input data x_i
b_j = bias for the neuron
n = number of input data

This sum X then passes through the transfer function F, which generates the output, as shown in Equation 17.

$$Y = F(x) = F\left[\left(\sum_{i=1}^{n} w_{ij} x_i \right) + b_j \right]$$

Equation 17

Hidden and output layers typically use linear or nonlinear activation functions. A common nonlinear function is the sigmoid, which compresses outputs to the range between 0 and 1, as shown in Equation 18.

$$F(X) = \frac{1}{1 + e^{-x}}$$

Equation 18

If the input and output layers have negative values, then the tansig transfer function is used, which is expressed as Equation 19.

$$F(X) = \frac{1 - e^{-2x}}{1 + e^{-2x}}$$

Equation 19

Table 4 provides a summary of the MLP architecture and its hyperparameters employed in this research.

3.3.4 Random Forest (RF)

Random Forest is a regression method that combines multiple Decision Trees (DTs) to predict a target variable. Given an input vector x with relevant features, RF builds K *r*egression trees and averages their outputs for prediction [58]. The RF predictor is defined in Equation 20.

$$f_{rf}^{K}(x) = \frac{1}{K}\sum_{k=1}^{K} T(x)$$

Equation 20

RF mitigates overfitting and enhances model generalisation by employing bagging a technique that constructs each decision tree using a distinct bootstrap sample drawn from the original dataset with replacement. This means individual samples may appear multiple times in a subset or not at all, introducing variance across trees and reducing correlation among them. Each model in the ensemble follows the form $\{h(x,\theta\_k), k = 1..., K\}$, where $\{\theta\_k\}$ represents an independently sampled random vector. This diversity improves robustness to input fluctuations and increases prediction accuracy, as demonstrated in prior studies [58]. Table 5 shows the Summary of RF architectures and parameters used in developing the model in this research.

3.3.5 Extreme Gradient Boosting (XGBoost)

XGBoost is a highly scalable gradient boosting framework that employs an ensemble of decision trees [59]. Like conventional gradient boosting, it incrementally optimises the objective function by minimising a specified loss function. However, as XGBoost exclusively uses decision trees as its base learners, a modified loss function is applied to regulate tree complexity, as illustrated in Equation 21.

$$L_{xgb} = \sum_{i=1}^{N} L\left(y_i, F\left(x_i\right)\right) + \sum_{m=1}^{M} \Omega\left(h_m\right)$$

Equation 21

Where:

$L(y_i, F(x_i))$ = loss function that measures the difference between the actual target and the predicted value $F(x_i)$

$\Omega(h_m)$ = regularisation term that controls the complexity of the base learners (typically, decision trees)

N = the total loss over all training samples

The sum over m = the total complexity penalty for all M weak learners.

The regularisation term used in XGBoost is expressed in Equation 22:

$$\Omega\left(h_m\right) = \gamma T + \frac{1}{2}\lambda\left\|w\right\|^2$$

Equation 22

Where:

T = number of leaves of the tree

w = output score of the leaves.

Table 6 presents a summary of the architecture and hyperparameters used for the XGBoost model.

Table 4: Summary of model architectures and parameters for MLPNN

Component	MLPNN
Architecture	Feedforward neural network
Hidden Layers	3 layers (8, 4, 2 neurons)
Feature Scaling	Min-Max Normalisation
Training Algorithm	Levenberg–Marquardt backpropagation (trainlm)
Loss Function	Mean Squared Error (MSE)
Learning Rate	0.001
Epochs	1 000
Training Goal	Performance goal of 1e−7

Table 5: Summary of model architectures and parameters for RF

Parameter	Implemented Setting
Model Type	Random Forest (TreeBagger)
Number of Trees	300 (Increased from 20)
Splitting Criterion	Mean Squared Error (MSE)
Min Leaf Size	3
Max Splits per Tree	50 (Manually set for better feature separation)
Feature Selection	Bagging (Bootstrap Aggregation)
Out-of-Bag (OOB) Prediction	Enabled
Base Learner	Decision Tree (Regression)
Learning Rate	Implicitly controlled via tree depth & feature bagging
Cross-Validation	5-Fold Applied
Surrogate Splitting	Enabled

Table 6: Summary of Model Architecture and Parameters for XGBoost

Parameter	XGBoost
Boosting Method	Extreme Gradient Boosting (XGBoost)
Objective Function	reg:squarederror
Number of Trees	300
Maximum Tree Depth	5
Learning Rate	0.05
Subsample Ratio	0.8
Column Sample by Tree	0.8
Feature Scaling	Min-Max Normalisation
Cross-Validation	Not Applied
Random Seed	42
Base Learner	Decision Tree

3.4 Model Selection Justification

The selection of models in this study was informed by both their established relevance in Zenith Tropospheric Delay (ZTD) prediction and the need to evaluate emerging neural architectures. XGBoost, Random Forest, Long Short-Term Memory (LSTM), and Multilayer Perceptron Neural Networks (MLPNN) have been widely employed in previous ZTD-related studies, demonstrating varying levels of predictive accuracy and robustness [60] [61] [62] and [63]. These models serve as representative baselines for ensemble learning methods (XGBoost and RF), recurrent neural networks (LSTM), and classical feedforward architectures (MLPNN).

In addition to these conventional models, this study incorporates and assesses the Kolmogorov Arnold Network, a recently proposed neural framework introduced by [41]. KAN is theoretically grounded in the Kolmogorov Arnold representation theorem and departs from traditional MLPs by replacing fixed linear weights with learnable univariate functions. These functions, implemented via adaptive spline transformations, allow KAN to approximate complex multivariate relationships with greater efficiency and flexibility [41]. This design renders KAN highly expressive while maintaining lower parameter complexity compared to deep multilayer networks.

Recent benchmarking studies have demonstrated that KAN not only outperforms conventional MLPs but also competes favourably with deeper architectures in domains such as mathematical modelling, partial differential equations, and time-series forecasting, all while utilising significantly fewer parameters [42] and [43]. Furthermore, KAN's white-box structure enhances model interpretability-an important consideration in geophysical applications such as ZTD prediction, where transparency and explainability are essential for operational trust and integration within GNSS-based systems [64].

3.5 Data Normalisation

To ensure constant variability in the dataset, normalisation is performed to scale the data into the ranges [-1, 1] and [0, 1]. Data normalisation improves convergence speed, thereby reducing the chances of getting stuck in local minima [65]. In this study, the input variables were normalised into the interval [-1, 1] using Equation 23 as follows:

$$y_i = y_{\min} + \frac{(y_{\max} - y_{\min})(x_i - x_{\min})}{x_{\max} - x_{\min}}$$

Equation 23

Where:

y_i = the normalised data
x_i = the measured ZTD data
x_{max} and x_{min} = the maximum and minimum values of the measured ZTD data
y_{max} and y_{min} = the values at 1 and -1, respectively

3.6 Network Training and Testing

To estimate the Zenith Tropospheric Delay (ZTD) using machine learning, this study employed a supervised learning framework to develop both deep learning and ensemble-based predictive models. Supervised learning, a common approach, allows models to learn mappings between inputs and outputs from labelled datasets. In this context, input features, including meteorological and geospatial variables, were used to predict corresponding ZTD values. To ensure the models' robustness and generalisability, the dataset was divided into two separate subsets: a training set and a testing set. This division followed the hold-out cross-validation method, a standard and effective technique in predictive modelling. Although there is no fixed ratio for train-to-test splitting, it is generally recommended that the training set be significantly larger than the test set, so the model can learn from a broader range of data patterns and improve its generalisation to unseen data. Table 7 lists the input and output parameters used across all models.

Table 7: Input and output parameters for all models

Variable Name	Symbol	Units	Function
Latitude	Φ	°	Input
Ellipsoidal Height	H	m	Input
Pressure	P	hPa	Input
Temperature	T	°C	Input
Relative Humidity	RH	%	Input
Zenith Total Delay	ZTD	m	Output

In this study, temporal segmentation was applied to maintain the dataset's chronological order, which is crucial for time-dependent predictions such as ZTD. Data from 2020 to 2021, making up about 70% of the dataset, were assigned to model training and optimisation. The remaining 30%, comprising data from 2022, was kept solely for testing. This temporal split supports an unbiased evaluation of model performance on future data, providing a realistic assessment of their use in operational GNSS applications.

3.7Model Performance Evaluators

The predictive accuracy of the models developed for estimating Zenith Tropospheric Delay (ZTD) was evaluated using three standard statistical metrics: Root Mean Square Error (RMSE), Mean Absolute Error (MAE), and the Coefficient of Determination (R^2). These metrics collectively offer a robust assessment of model accuracy, consistency, and explanatory power:

- Root Mean Square Error (RMSE) reflects the square root of the mean of squared differences between predicted and actual values. It places greater emphasis on large errors, making it sensitive to outliers.
- Mean Absolute Error (MAE) represents the average of the absolute differences between predicted and actual values, providing an intuitive measure of the typical prediction error.
- Coefficient of Determination (R^2) indicates the proportion of variance in the actual data that is captured by the model's predictions. Values closer to 1 signify better model performance.

The mathematical formulations of these performance metrics are presented in Equations (24) to (26):

$$RMSE = \sqrt{\frac{1}{n}\sum_{i=1}^{n}\left(o_i - p_i\right)^2}$$

Equation 24

$$MAE = \frac{1}{n}\sum_{i=1}^{n}\left|o_i - p_i\right|$$

Equation 25

$$R^2 = \frac{\left(\sum_{i=1}^{n}(o_i - \bar{o})(p_i - \bar{p})\right)^2}{\sum_{i=1}^{n}(o_i - \bar{o})^2 \times \sum_{i=1}^{n}(p_i - \bar{p})^2}$$

Equation 26

Where:

N = total number of test samples
o_i = observed values
p = predicted values,
$\bar{o}$ = mean of the observed values
$\bar{p}$= mean of the predicted values

These metrics were computed for both the training and testing datasets to assess not only the goodness-of-fit during training but also the generalisability of the models to unseen data. The comparative analysis based on these metrics enabled the identification of the most effective model for accurate ZTD prediction.

4. Results and Discussion

4.1 Daily Variation of Observed and Predicted ZTD

The daily variations of observed ZTD and the corresponding predicted values for the year 2022 at each GNSS CORS station are presented in Figures 5 to 8. All models demonstrated a high degree of agreement with the observed ZTD, closely tracking the temporal patterns with minimal deviations. The Kolmogorov Arnold Network (KAN) and Long Short-Term Memory (LSTM) models exhibited strong generalisation capabilities across all stations, effectively capturing both high-frequency fluctuations and broader seasonal trends. Ensemble-based models, including XGBoost and Random Forest, also yielded competitive results, with slightly improved alignment during periods of lower atmospheric variability. At the Accra station (Figure 5), all models successfully reproduced the seasonal dynamics, with KAN and XGBoost closely matching the observed peaks and troughs.

The Ho station (Figure 6) exhibited slightly more frequent variations, but model performance remained robust, particularly for KAN and LSTM. In Kumasi (Figure 7), where atmospheric variability was more pronounced, prediction accuracy was slightly reduced, though KAN and LSTM still maintained reasonable performance. In Figure 8 at Akim Oda, all models capture the overall trends, but KAN and LSTM deliver the most precise and consistent predictions. Random Forest and XGBoost exhibit minor deviations, particularly during periods of rapid atmospheric change.

4.2 Comparative Performance of Developed Models

The comparative performance of the predictive models was evaluated using statistical metrics, including RMSE, MAE, and R^2. The results obtained for each model across the GNSS CORS stations are summarised in Table 8. These metrics provide a comprehensive assessment of each model's predictive accuracy and generalisation capability. Observing from Table 8, KAN achieved the highest predictive performance across all evaluated GNSS stations, with RMSE values of approximately 10 mm and R^2 between 0.976 and 0.977. MLPNN and LSTM networks followed KAN by recording RMSEs between 10.0 mm and 10.9 mm, with R^2 values averaging around 0.974. Although MLPNN and LSTM are well-established for nonlinear regression and temporal modelling, respectively, KAN outperformed both by offering efficient, transparent modelling of nonlinear ZTD patterns with fewer parameters and stronger generalisation, particularly in tropical environments.

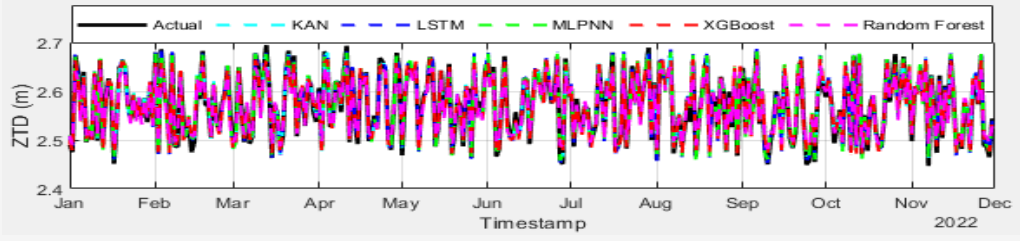

Figure 5: Daily variation of actual and predicted ZTD values at Accra CORS (2022)

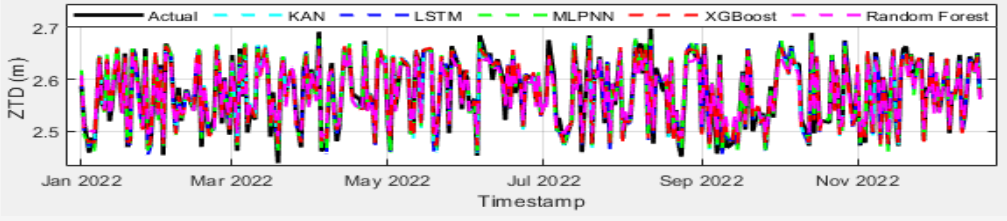

Figure 6: Daily variation of actual and predicted ZTD values at Ho CORS (2022)

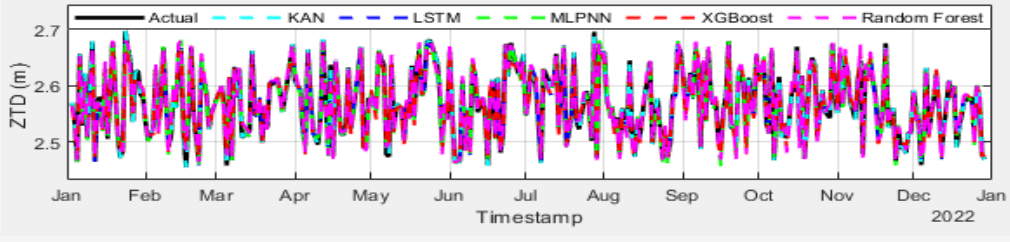

Figure 7: Daily variation of actual and predicted ZTD values at Kumasi CORS (2022)

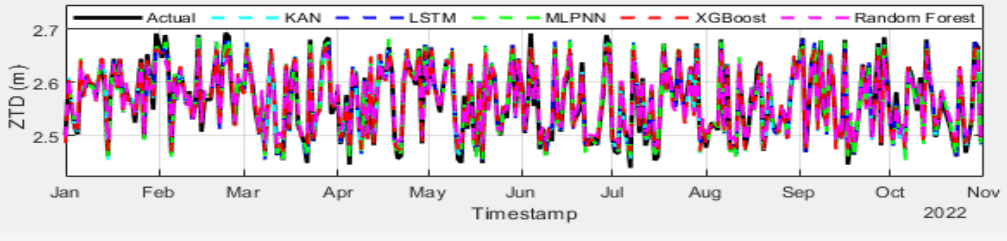

Figure 8: Daily variation of actual and predicted ZTD values at Akim Oda CORS (2022)

Table 8: Comparative performance of machine learning models across GNSS stations

Station	Model	RMSE (Train) (mm	RMSE (Test) (mm)	MAE (Train) (mm)	MAE (Test) (mm)	R^2 (Train)	R^2 (Test)
	KAN	**10.10**	**10.00**	**8.00**	**8.00**	**0.976**	**0.977**
	MLPNN	10.30	10.40	8.50	8.60	0.974	0.974
Accra	LSTM	10.40	10.60	8.40	8.70	0.974	0.974
	XGBoost	10.70	11.60	8.10	9.20	0.975	0.966
	Random Forest	12.10	16.40	9.30	13.00	0.967	0.944
	KAN	**10.10**	**10.10**	**8.00**	**8.10**	**0.976**	**0.977**
	MLPNN	10.20	10.20	8.30	8.30	0.976	0.976
Ho	LSTM	10.40	10.40	8.20	8.40	0.975	0.977
	XGBoost	10.70	11.70	8.30	9.10	0.973	0.970
	Random Forest	13.20	18.20	10.30	14.60	0.959	0.928
	KAN	**10.00**	**10.10**	**8.10**	**8.10**	**0.977**	**0.975**
	MLPNN	10.30	10.50	8.40	8.40	0.977	0.972
Kumasi	LSTM	10.20	10.40	8.00	8.40	0.977	0.971
	XGBoost	11.00	12.10	8.40	9.60	0.973	0.966
	Random Forest	15.30	19.60	12.00	15.60	0.948	0.902
	KAN	**10.10**	**10.20**	**8.10**	**8.10**	**0.977**	**0.976**
Akim	MLPNN	10.50	10.90	8.30	8.60	0.975	0.975
Oda	LSTM	10.40	10.80	8.20	8.70	0.975	0.974
	XGBoost	10.40	12.00	8.10	9.30	0.975	0.968
	Random Forest	15.40	18.10	12.00	13.80	0.946	0.930

As seen in Table 8 again, XGBoost achieved slightly lower performance, with test RMSEs ranging from 11.6 mm to 12.1 mm and R^2 between 0.965 and 0.970. While XGBoost is known for its strong performance on structured, tabular datasets, it lacks native mechanisms for modelling sequential or temporal dependencies, an important limitation when predicting time-dependent atmospheric phenomena such as ZTD. The Random Forest model recorded the weakest performance among the evaluated models, with test RMSE values reaching up to 19.6 mm and R^2 values dropping to 0.901 in some stations, notably Kumasi (Table 8). This result is consistent with broader observations in the literature that ensemble tree models often struggle with generalisation when dealing with continuous temporal dynamics [66].

4.3 Comparative Analysis in Light of Existing ZTD Literature

Compared to prior neural networks, hybrid models, and ensemble models, KAN delivered comparable or superior accuracy with fewer parameters and better generalisation, particularly under tropical conditions. For example, a hybrid LSTM–RBF approach applied to 65 Antarctic stations reported RMSEs ranging from 6.4 mm to 32.8 mm (mean 10.9 mm) [67]. Similarly, a convolutional LSTM (TropNet) achieved ~11.5 mm RMSE for 6-hour ZWD forecasts in the U.S. [68], while global ZTD residual prediction using LSTM produced RMSEs around 14.4 mm on unseen 2020 data [69]. An LSTM-encoder model using GPT3 input achieved 14.43 mm RMSE and 0.95 R^2 across 178 Australian stations [70]. A hybrid Informer–LSTM model was used to predict ZTD at 11 stations in Europe, achieving 19.1 mm RMSE, 14.5 mm MAE, and 0.916 R^2 [71]. MLP model achieved RMSEs between 20 and 30 mm for short-term ZTD prediction across Europe [37]. A 1D CNN trained on radiosonde-based ZWD data reported RMSEs from 26.9 to 42.9 mm [72]. XGBoost modelled Zenith Wet Delay (ZWD), yielding RMSEs between 10.1 mm and 16.2 mm [73]. Random Forest predicted global ZWD with RMSEs of 31 mm (radiosonde) and 24 mm (GPS-RO) [74]. A hybrid RF + CNN model for ZTD in China achieved 32.4 mm RMSE [75].

Despite the strong performance of deep learning approaches and ensemble models, KAN stands out for its unique balance of predictive power, efficiency, and interpretability. Its ability to achieve competitive results with fewer parameters enhances its suitability for data-scarce or tropical regions where both model robustness and transparency are critical.

5. Conclusion

This study demonstrated the application of advanced ML models to accurately predict ZTD over selected GNSS CORS sites in Ghana. Among the models evaluated are KAN, LSTM, MLPNN, XGBoost, and Random Forest. KAN consistently exhibited superior performance across all locations, achieving test RMSE values around 10 mm and R^2 exceeding 0.976. This outcome underscores the efficacy of spline-activated architectures like KAN in modelling complex, nonlinear atmospheric patterns, particularly in tropical environments. LSTM and MLPNN models also delivered competitive results with RMSE values between 10.0–10.9 mm and $R^2 \approx 0.974$, validating their relevance for ZTD forecasting. In contrast, ensemble models such as XGBoost and Random Forest, though effective on tabular data, showed relatively limited ability to model temporal dependencies inherent in tropospheric dynamics, reflected in higher RMSEs of up to 19.6 mm and reduced generalisation, particularly for Random Forest.

Furthermore, the uniformity of model performance across stations highlights the shared meteorological patterns typical of Ghana's tropical climate. However, localised variations, particularly observed in Kumasi, may be attributed to microclimatic influences or unresolved spatial heterogeneity. Future enhancements could consider integrating additional spatial metadata such as land cover type or vegetation indices (e.g., NDVI). Prior studies have demonstrated that surface characteristics, including vegetation density and land use, influence near-surface atmospheric moisture content and can affect GNSS-derived ZTD estimates. Incorporating such geospatial indicators may improve model responsiveness to local land atmosphere interactions, particularly in heterogeneous or semi-urban terrains.

It is also crucial to acknowledge a key limitation of this study: the geographic confinement of the dataset. All GNSS stations used for training and validation are located within Ghana, situated in the equatorial low-latitude zone (approximately 4.5°N to 7.5°N). Consequently, the models were trained solely on data reflecting tropical climatic conditions and may not generalise effectively to other regions, especially subtropical high-pressure zones or subpolar regions where meteorological variables such as pressure, temperature, and relative humidity follow different dynamics. As machine learning models are inherently data-driven and lack physical interpretability, they are known to perform poorly when extrapolating beyond their training data. This limitation underscores the importance of retraining or validating such models with region-specific data before applying them operationally outside tropical environments.

Moreover, machine learning should be recognised as a powerful numerical tool rather than a physically grounded scientific model. While it enables the capture of nonlinear and complex patterns in data, its predictions are heavily contingent on the quality, quantity, and representativeness of training data. As such, results should always be interpreted with an understanding of these constraints, particularly in scientific contexts where interpretability, causality, and physical generalisation are essential.

References

[1] Altamimi, Z., Rebischung, P., Métivier, L. and Collilieux, X., (2016). ITRF2014: A New Release of the International Terrestrial Reference Frame Modelling Nonlinear Station Motions. *Journal of Geophysical Research: Solid Earth*, Vol. 121(8), 6109–6131. https://doi.org/10.1002/2016jb013098.

[2] Zhao, J., Song, S., Chen, Q., Zhou, W. and Zhu, W., (2014). Establishment of a New Global Model for Zenith Tropospheric Delay Based on Functional Expression for Its Vertical Profile. *Chinese Journal of Geophysics*, Vol. 57(10), 3140–3153.

[3] Zhang, H., Yuan, Y., Li, W., Zhang, B. and Ou, J., (2017). A Grid-Based Tropospheric Product for China Using a GNSS Network. *Journal of Geodesy*, Vol. 92(7), 765–777. https://doi.org/10.1007/s00190-017-1093-z.

[4] Jin, S. and Su, K., (2020). PPP Models and Performances from Single to Quad-Frequency BDS Observations. *Satellite Navigation*, Vol. 1(1). https://doi.org/10.1186/s43020-020-00014-y.

[5] Thammaboribal, P., Tripathi, N., Nakamura, S., and Lipiloet, S. (2025). Determinations of the Slope of the Chao Phraya Riverbank and Manning's Roughness Coefficient Utilizing Precise Point Positioning (PPP) Measurement Technique. *International Journal of Geoinformatics*, Vol. 21(2), 141–158. https://doi.org/10.52939/ijg.v21i2.3953.

[6] Zhou, F., Cao, X., Ge, Y. and Li, W., (2019). Assessment of the Positioning Performance and Tropospheric Delay Retrieval with Precise Point Positioning Using Products from Different Analysis Centres. *GPS Solutions*, Vol. 24(1). https://doi.org/10.1007/s10291-019-0925-0.

[7] Zhu, G., Huang, L., Liu, L., Li, C., Li, J., Huang, L., Zhou, L. and He, H., (2021). A New Approach for the Development of Grid Models Calculating Tropospheric Key Parameters over China. *Remote Sensing*, Vol. 13(17), 3546–3546. https://doi.org/10.3390/rs13173546

[8] Huang, L., Mo, Z., Xie, S., Liu, L., Chen, J., Kang, C. and Wang, S., (2021). Spatiotemporal Characteristics of GNSS-derived Precipitable Water Vapour During Heavy Rainfall Events in Guilin, China. *Satellite Navigation*, Vol. 2(1). https://doi.org/10.1186/s43020-021-00046-y.

[9] Mohammed, J. (2022). Adaptive Neuro Fuzzy Inference System for Predicting Sub-Daily Zenith Wet Delay. *Geodesy and Geodynamics*. https://doi.org/10.1016/j.geog.2021.10.005.

[10] Molteni, F., Buizza, R., Palmer, T. N. and Petroliagis, T., (1996). The ECMWF Ensemble Prediction System: Methodology and validation. *Quarterly Journal of the Royal Meteorological Society*, Vol. 122(529), 73–119. https://doi.org/10.1002/qj.49712252905.

[11] Bauer, P., Thorpe, A. and Brunet, G., (2015). The Quiet Revolution of Numerical Weather Prediction. *Nature*, Vol. 525(7567), 47–55. https://doi.org/10.1038/nature14956.

[12] Huang, L., Chen, H., Liu, L. and Jiang, W., (2021a). A New High-Precision Global Model for Calculating Zenith Tropospheric Delay. *Chinese Journal of Geophysics*, Vol. 64(3), 782–795.

[13] Kanamitsu, M., (1989). Description of the NMC Global Data Assimilation and Forecast System. *Weather and Forecasting*, Vol. 4(3), 335–342.

[14] Hopfield, H. S., (1969). Two-quartic Tropospheric Refractivity Profile for Correcting Satellite Data. *Journal of Geophysical Research*, Vol. 74(18), 4487–4499. https://doi.org/10.1029/jc074i018p04487

[15] Saastamoinen, J., (2013). Atmospheric Correction for the Troposphere and Stratosphere in Radio Ranging Satellites. *Geophysical Monograph,* Vol. 15, 247–251. https://doi.org/10.1029/gm015p0247.

[16] Black, H. D., (1978). An Easily Implemented Algorithm for the Tropospheric Range Correction. *Journal of Geophysical Research: Solid Earth*, Vol. 83(B4), 1825–1828. https://doi.org/10.1029/jb083ib04p01825.

[17] Leandro, R. F., Langley, R. B., and Santos, M. C., (2007). UNB3m_Pack: A Neutral Atmosphere Delay Package for Radiometric Space Techniques. *GPS Solutions*, Vol. 12(1), 65–70. https://doi.org/10.1007/s10291-007-0077-5.

[18] Penna, N., Dodson, A., and Chen, W., (2001). Assessment of EGNOS Tropospheric Correction Model. *Journal of Navigation*, Vol. 54(1), 37–55. https://doi.org/10.1017/s0373463300001107.

[19] Krueger, E., Schüler, T., Hein, G. W., Martellucci, A. and Blarzino, G., (2004). Galileo Tropospheric Correction Approaches Developed within GSTB-V1. *In Proceedings of ENC-GNSS 2004*, 16–19.

[20] Schüler, T., (2013). The TropGrid2 Standard Tropospheric Correction Model. *GPS Solutions*, Vol. 18(1), 123–131. https://doi.org/10.1007/s10291-013-0316-x.

[21] Boehm, J., Heinkelmann, R. and Schuh, H., (2007). Short Note: A global model of Pressure and Temperature for Geodetic Applications. *Journal of Geodesy*, Vol. 81(10), 679–683. https://doi.org/10.1007/s00190-007-0135-3.

[22] Böhm, J., Möller, G., Schindelegger, M., Pain, G. and Weber, R., (2015). Development of an Improved Blind Model for Slant Delays in the Troposphere (GPT2w). *GPS Solutions*, Vol. 19(3), 433–441. https://doi.org/10.1007/s10291-014-0403-7.

[23] Lagler, K., Schindelegger, M., Johannes Böhm, Krásná, H., and Nilsson, T., (2013). GPT2: Empirical Slant Delay Model for Radio Space Geodetic Techniques. *Geophysical Research Letters*, Vol. 40(6), 1069–1073. https://doi.org/10.1002/grl.50288.

[24] Landskron, D. and Böhm, J., (2018). VMF3/GPT3: Refined Discrete and Empirical Troposphere Mapping Functions. *Journal of Geodesy*, Vol. 92(4), 349–360. https://doi.org/10.1007/s00190-017-1066-2.

[25] Lu, C., Zhong, Y., Wu, Z., Zheng, Y. and Wang, Q., (2023). A Tropospheric Delay Model to Integrate ERA5 and GNSS Reference Network for Mountainous Areas: Application to Precise Point Positioning. *GPS Solutions*, Vol. 27(2). https://doi.org/10.1007/s10291-023-01425-5.

[26] Pikridas, C., Katsougiannopoulos, S. and Ifadis, I. M., (2010). Predicting Zenith Tropospheric Delay using the Artificial Neural Network technique. Application to selected EPN stations. *Journal of the National Cancer Institute*, Vol. 88(24), 1803–1805.

[27] Ssenyunzi, R. C., Andima, G. and Habyarimana, V., (2025). Enhancing the Prediction of Zenith Tropospheric Delay using VMF3 Products and Artificial Neural Networks Over the African Tropical Region. [Online]. Available: https://doi.org/10.2139/ssrn.5352083. [Accessed Aug. 2, 2025].

[28] Huang, L., Bi, H., Zhang, H., Wang, S., Liao, F., Liu, L. and Jiang, W., (2024). An Optimised BP Neural Network for Modelling Zenith Tropospheric Delay in the Chinese Mainland Using Coupled Particle Swarm and Genetic Algorithm. *Geo-Spatial Information Science*, 1–16. https://doi.org/10.1080/10095020.2024.2392701.

[29] Zheng, D. Y., Hu, W. S., Wang, J. and Zhu, M. C., (2014). Research on Regional Zenith Tropospheric Delay Based on Neural Network Technology. *Survey Review*, Vol. 47(343), 286–295. https://doi.org/10.1179/1752270614y.0000000130.

[30] Ding, M., Hu, W., Jin, X., and Yu, L., (2016). A New ZTD Model Based on Permanent Ground-Based GNSS-ZTD data. *Survey Review*, Vol. 48(351), 385–391. https://doi.org/10.1179/1752270615y.0000000034.

[31] Ding, M. and Hu, W., (2018). Erratum and Addendum to the Paper "A New ZTD Model Based on Permanent Ground-Based GNSS-ZTD Data", Survey Review, 2016, 48(351), 385–391. *Survey Review*, Vol. 51(366), 280–287. https://doi.org/10.1080/00396265.2017.1420585.

[32] Yang, Y., Xu, T. and Ren, L., (2017). A New Regional Tropospheric Delay Correction Model Based on BP Neural Network. In *2017 Forum on Cooperative Positioning and Service (CPGPS)*, 96–100. https://doi.org/10.1109/CPGPS.2017.8075104.

[33] Selbesoglu, M. O., (2020). Prediction of Tropospheric Wet Delay by an Artificial Neural Network Model Based on Meteorological and GNSS Data. *Engineering Science and Technology, an International Journal*, Vol. 23(5), 967–972. https://doi.org/10.1016/j.jestch.2019.11.006.

[34] Zhang, Q., Li, F., Zhang, S. and Li, W., (2020). Modelling and Forecasting the GPS Zenith Troposphere Delay in West Antarctica Based on Different Blind Source Separation Methods and Deep Learning. *Sensors*, Vol. 20(8). https://doi.org/10.3390/s20082343.

[35] Zhang, H., Yao, Y., Hu, M., Xu, C., Su, X., Che, D. and Peng, W., (2022). A Tropospheric Zenith Delay Forecasting Model Based on a Long Short-Term Memory Neural Network and Its Impact on Precise Point Positioning. *Remote Sensing*, Vol. 14(23), 5921–5921. https://doi.org/10.3390/rs14235921.

[36] Li, L., Xu, Y., Yan, L., Wang, S., Liu, G. and Liu, F., (2020). A Regional NWP Tropospheric Delay Inversion Method Based on a General Regression Neural Network Model. *Sensors*, Vol. 20(11), 3167. https://doi.org/10.3390/s20113167.

[37] Katsougiannopoulos, S. and Pikridas, C., (2009). Prediction of Zenith Tropospheric Delay by Multi-Layer Perceptron. *Journal of Applied Geodesy*, Vol. 3(4). https://doi.org/10.1515/jag.2009.022.

[38] Zaremba, W., Sutskever, I. and Vinyals, O., (2014). *Recurrent Neural Network Regularisation*. Cornell University. [Online]. Available: https://doi.org/10.48550/arxiv.1409.2329. [Accessed Aug. 7, 2025].

[39] Rudin, C., Chen, C., Chen, Z., Huang, H., Semenova, L. and Zhong, C., (2022). Interpretable Machine Learning: Fundamental Principles and 10 Grand Challenges. *Statistics Surveys*, Vol. 16. https://doi.org/10.1214/21-ss133.

[40] Haddouchi, M., and Berrado, A., (2024). A Survey and Taxonomy of Methods Interpreting Random Forest Models. *arXiv*. https://doi.org/10.48550/arXiv.2407.12759.

[41] Liu, Z., Wang, Y., Vaidya, S., Ruehle, F., Halverson, J., Soljačić, M., Hou, T. Y. and Tegmark, M., (2024). *KAN: Kolmogorov–Arnold networks.* Cornell University. [Online]. Available: https://arxiv.org/abs/2404.19756. [Accessed Aug. 2, 2025].

[42] Shukla, K., Toscano, J. D., Wang, Z., Zou, Z. and Karniadakis, G. E., (2024). A Comprehensive and FAIR Comparison between MLP and KAN Representations for Differential Equations and Operator Networks. *Computer Methods in Applied Mechanics and Engineering*, Vol. 431, 117290–117290. https://doi.org/10.1016/j.cma.2024.117290.

[43] Pant, N., He, S., Wang, X. and Chen, Y., (2025). *MLPs and KANs for Data-Driven Learning in Physical Problems: A Performance Comparison.* Cornell University. [Online]. Available: https://arxiv.org/abs/2504.11397. [Accessed: Aug. 2, 2025].

[44] Yuan, Z., Lin, X., Xu, Y., Zhao, J., Du, N., Cai, X. and Li, M., (2024). Zenith Tropospheric Delay Forecasting in the European Region Using the Informer–Long Short-Term Memory Networks Hybrid Prediction Model. *Atmosphere*, Vol. 16(1), 31–31. https://doi.org/10.3390/atmos16010031.

[45] Crocetti, L., Schartner, M., Zus, F., Zhang, W., Möller, G., Navarro, V., See, L., Schindler, K. and Soja, B., (2024). Global, Spatially Explicit Modelling of Zenith Wet Delay with XGBoost. *Journal of Geodesy*, Vol. 98(4). https://doi.org/10.1007/s00190-024-01829-2.

[46] Li, Q., Böhm, J., Yuan, L., and Weber, R., (2024). Global Zenith Wet Delay Modelling with Surface Meteorological Data and Machine Learning. *GPS Solutions*, Vol. 28(1). https://doi.org/10.1007/s10291-023-01595-2.

[47] Smith, E. K. and Weintraub, S., (1953). The Constants in the Equation for Atmospheric Refractive Index at Radio Frequencies. *Journal of Research of the National Bureau of Standards*, Vol. 50(1), 39. https://doi.org/10.6028/jres.050.006.

[48] Lo, J. and El-Mowafy, A., (2012). An Investigation into the Correlations Among GNSS Observations and their Impact on Height and Zenith Wet Delay Estimation for Medium and Long Baselines. *Geo-Spatial Information Science*, Vol. 15(4), 219–228. https://doi.org/10.1080/10095020.2012.745051.

[49] Yuan, Y., Holden, L., Kealy, A., Choy, S. and Hordyniec, P., (2019). Assessment of Forecast Vienna Mapping Function 1 For Real-Time Tropospheric Delay Modelling in GNSS. *Journal of Geodesy*, Vol. 93(9),1501–1514. https://doi.org/10.1007/s00190-019-01263-9.

[50] Bevis, M., Businger, S., Chiswell, S. M., Herring, T. A., Anthes, R. A., Rocken, C. and Ware, R., (1994). GPS Meteorology: Mapping Zenith Wet Delays onto Precipitable Water. *Journal of Applied Meteorology*, Vol. 33(3), 379–386. https://doi.org/10.1175/1520-0450(1994)033%3C0379:gmmzwd%3E2.0.co;2.

[51] Chen, Q., Song, S., Heise, S., Liou, Y. A., Zhu, W. and Zhao, J., (2011). Assessment of ZTD Derived from ECMWF/NCEP data with GPS ZTD over China. *GPS Solutions*, Vol. 15(4), 415–425. https://doi.org/10.1007/s10291-010-0200-x.

[52] Smith, E. K. and Weintraub, S., (1953). The Constants in the Equation for Atmospheric Refractive Index at Radio Frequencies. *Journal of Research of the National Bureau of Standards*, Vol. 50(1), 39–39. https://doi.org/10.6028/jres.050.006.

[53] Feng, P., Li, F., Yan, J., Zhang, F. and Barriot, J. P., (2020). Assessment of the Accuracy of the Saastamoinen Model and VMF1/VMF3 Mapping Functions with Respect to Ray-Tracing from Radiosonde Data in the Framework of GNSS Meteorology. *Remote Sensing*, Vol. 12(20). https://doi.org/10.3390/rs12203337.

[54] Saastamoinen. J., (2013). Atmospheric Correction for the Troposphere and Stratosphere in Radio Ranging Satellites. 247–251. https://doi.org/10.1029/gm015p0247.

[55] Kundu, A., Sarkar, A. and Sadhu, A., (2024). KANQAS: Kolmogorov-Arnold Network for Quantum Architecture Search. *EPJ Quantum Technology*, Vol. 11(1). https://doi.org/10.1140/epjqt/s40507-024-00289-z.

[56] Zhang, H., Yao, Y., Hu, M., Xu, C., Su, X., Che, D. and Peng, W., (2022). A Tropospheric Zenith Delay Forecasting Model Based on a Long Short-Term Memory Neural Network and Its Impact on Precise Point Positioning. *Remote Sensing*, Vol. 14(23), 5921–5921. https://doi.org/10.3390/rs14235921.

[57] Konakoğlu, B., (2021). Prediction of geodetic point velocity using MLPNN, GRNN, and RBFNN Models: A Comparative Study. *Acta Geodaetica et Geophysica*, Vol. 56(2), 271–291. https://doi.org/10.1007/s40328-021-00336-6.

[58] Rodriguez-Galiano, V., Sanchez-Castillo, M., Chica-Olmo, M. and Chica-Rivas, M., (2015). Machine Learning Predictive Models for Mineral Prospectivity: An Evaluation of Neural Networks, Random Forest, Regression Trees and Support Vector Machines. *Ore Geology Reviews*, Vol. 71(71), 804–818. https://doi.org/10.1016/j.oregeorev.2015.01.001.

[59] Kulpanich, N., Worachairungreung, M., Thanakunwutthirot, K., and Chaiboonrueang, P. (2023). The Application of Unmanned Aerial Vehicles (UAVs) and Extreme Gradient Boosting (XGBoost) to Crop Yield Estimation: A Case Study of Don Tum District, Nakhon Pathom, Thailand. *International Journal of Geoinformatics*, Vol. 19(2), 65–77. https://doi.org/10.52939/ijg.v19i2.2569.

[60] Li, Q., Johannes Böhm, Yuan, L. and Weber, R. (2024). Global Zenith Wet Delay Modelling with Surface Meteorological Data and Machine Learning. *GPS Solutions*, Vol. 28(1). https://doi.org/10.1007/s10291-023-01595-2.

[61] He, L., Yao, Y., Xu, C., Zhang, H., Tang, F., Ji, C., Liu, Z. and Wu, W., (2024). A New Global ZTD Forecast Model Based on Improved LSTM Neural Network. *IEEE Journal of Selected Topics in Applied Earth Observations and Remote Sensing*, Vol. 17, 9606–9614. https://doi.org/10.1109/jstars.2024.3391821.

[62] Crocetti, L., Schartner, M., Wareyka-Glaner, M. F., Schindler, K. and Soja, B., (2024). ZWDX: A Global Zenith Wet Delay Forecasting Model using XGBoost. *Earth Planets and Space*, Vol. 76(1). https://doi.org/10.1186/s40623-024-02104-6.

[63] Katsougiannopoulos, S., and Pikridas, C., (2010). Prediction of Zenith Tropospheric Delay by Multi-Layer Perceptron. *Journal of Applied Geodesy*, Vol. 4, 223–229. https://doi.org/10.1515/JAG.2009.022.

[64] Xu, K., Chen, L. and Wang, S., (2024). Kolmogorov Arnold Networks for Time Series: Bridging Predictive Power and Interpretability. Cornell University. [Online]. Available: https://arxiv.org/abs/2406.02496. [Accessed Aug. 2, 2025].

[65] Ziggah, Y. Y., Youjian, H., Yu, X. and Basommi, L. P., (2016). Capability of Artificial Neural Network for Forward Conversion of Geodetic Coordinates (ϕ, λ, h) to Cartesian Coordinates (X, Y, Z). *Mathematical Geosciences*, Vol. 48(6), 687–721. https://doi.org/10.1007/s11004-016-9638-x.

[66] Zhu, T., (2020). Analysis on the Applicability of the Random Forest. *Journal of Physics: Conference Series*, Vol. 1607(1), 012123. https://doi.org/10.1088/1742-6596/1607/1/012123.

[67] He, L., Yao, Y., Xu, C., Zhang, H., Tang, F., Ji, C., Liu, Z. and Wu, W., (2024). A New Global ZTD Forecast Model Based on Improved LSTM Neural Network. *IEEE Journal of Selected Topics in Applied Earth Observations and Remote Sensing*, Vol. 17, 9606–9614. https://doi.org/10.1109/jstars.2024.3391821.

[68] Li, S., Xu, T., Xu, Y., Jiang, N. and Bastos, L., (2022). Forecasting GNSS Zenith Troposphere Delay by Improving GPT3 Model with Machine Learning in Antarctica. *Atmosphere*, Vol. 13(1), 78–78. https://doi.org/10.3390/atmos13010078.

[69] Lu, C., Zheng, Y., Wu, Z., Zhang, Y., Wang, Q., Wang, Z., Liu, Y. and Zhong, Y., (2023). TropNet: A Deep Spatiotemporal Neural Network for Tropospheric Delay Modelling and Forecasting. *Journal of Geodesy*, Vol. 97(4). https://doi.org/10.1007/s00190-023-01722-4.

[70] Peng, Y., Cai, C., Li, Z., Kaihui L, Zhang, X. and Cai, Y., (2025). Regional Tropospheric Delay Prediction Model Based on LSTM-Enhanced Encoder Network. *IEEE Journal of Selected Topics in Applied Earth Observations and Remote Sensing*, 1–11. https://doi.org/10.1109/jstars.2025.3565569.

[71] Yuan, Z., Lin, X., Xu, Y., Zhao, J., Du, N., Cai, X. and Li, M., (2024). Zenith Tropospheric Delay Forecasting in the European Region Using the Informer–Long Short-Term Memory Networks Hybrid Prediction Model. *Atmosphere,* Vol. 16(1) 31. https://doi.org/10.3390/atmos16010031.

[72] Bi, H., Huang, L., Zhang, H., Xie, S., Zhou, L. and Liu, L., (2024). A Deep Learning-Based Model for Tropospheric Wet Delay Prediction Based on Multi-Layer 1D Convolution Neural Network. *Advances in Space Research*, Vol. 73(10), 5031–5042. https://doi.org/10.1016/j.asr.2024.02.039.

[73] Crocetti, L., Schartner, M., Wareyka-Glaner, M. F., Schindler, K. and Soja, B., (2024). ZWDX: A Global Zenith Wet Delay Forecasting Model using XGBoost. *Earth Planets and Space*, Vol. 76(1). https://doi.org/10.1186/s40623-024-02104-6.

[74] Li, Q., Böhm, J., Yuan, L. and Weber, R., (2024). Global Zenith Wet Delay Modelling with Surface Meteorological Data and Machine Learning. *GPS Solutions*, Vol. 28(1). https://doi.org/10.1007/s10291-023-01595-2.

[75] Zhang, J., Liang, Q. and Huang, Y., (2024). New Models of Zenith Tropospheric Delay for Chinese Mainland and Surrounding Areas Based on Convolutional Neural Network and Random Forest. *IEEE Access*, Vol. 12, 112864–112880. https://doi.org/10.1109/access.2024.3441331.